



**HAL**  
open science

## Large Magnetoresistance of Isolated Domain Walls in $\text{La}_{2/3}\text{Sr}_{1/3}\text{MnO}_3$ Nanowires

Gloria Orfila, David Sanchez-manzano, Ashima Arora, Fabian Cuellar, Sandra Ruiz-gómez, Sara Rodriguez-corvillo, Sandra López, Andrea Peralta, Santiago J Carreira, Fernando Gallego, et al.

► **To cite this version:**

Gloria Orfila, David Sanchez-manzano, Ashima Arora, Fabian Cuellar, Sandra Ruiz-gómez, et al.. Large Magnetoresistance of Isolated Domain Walls in  $\text{La}_{2/3}\text{Sr}_{1/3}\text{MnO}_3$  Nanowires. *Advanced Materials*, 2023, 35 (33), 10.1002/adma.202211176 . hal-04303170

**HAL Id: hal-04303170**

<https://hal.science/hal-04303170v1>

Submitted on 23 Nov 2023

**HAL** is a multi-disciplinary open access archive for the deposit and dissemination of scientific research documents, whether they are published or not. The documents may come from teaching and research institutions in France or abroad, or from public or private research centers.

L'archive ouverte pluridisciplinaire **HAL**, est destinée au dépôt et à la diffusion de documents scientifiques de niveau recherche, publiés ou non, émanant des établissements d'enseignement et de recherche français ou étrangers, des laboratoires publics ou privés.



Distributed under a Creative Commons Attribution 4.0 International License

# Large Magnetoresistance of Isolated Domain Walls in $\text{La}_{2/3}\text{Sr}_{1/3}\text{MnO}_3$ Nanowires

Gloria Orfila, David Sanchez-Manzano, Ashima Arora, Fabian Cuellar, Sandra Ruiz-Gómez, Sara Rodriguez-Corvillo, Sandra López, Andrea Peralta, Santiago J. Carreira, Fernando Gallego, Javier Tornos, Victor Rouco, Juan J. Riquelme, Carmen Munuera, Federico J. Mompean, Mar Garcia-Hernandez, Zouhair Sefrioui, Javier E. Villegas, Lucas Perez, Alberto Rivera-Calzada, Carlos Leon, Sergio Valencia,\* and Jacobo Santamaria

Generation, manipulation, and sensing of magnetic domain walls are cornerstones in the design of efficient spintronic devices. Half-metals are amenable for this purpose as large low field magnetoresistance signals can be expected from spin accumulation at spin textures. Among half metals,  $\text{La}_{1-x}\text{Sr}_x\text{MnO}_3$  (LSMO) manganites are considered as promising candidates for their robust half-metallic ground state, Curie temperature above room temperature ( $T_c = 360$  K, for  $x = 1/3$ ), and chemical stability. Yet domain wall magnetoresistance is poorly understood, with large discrepancies in the reported values and conflicting interpretation of experimental data due to the entanglement of various source of magnetoresistance, namely, spin accumulation, anisotropic magnetoresistance, and colossal magnetoresistance. In this work, the domain wall magnetoresistance is measured in LSMO cross-shape nanowires with single-domain walls nucleated across the current path. Magnetoresistance values above 10% are found to be originating at the spin accumulation caused by the mistracking effect of the spin texture of the domain wall by the conduction electrons. Fundamentally, this result shows the importance on non-adiabatic processes at spin textures despite the strong Hund coupling to the localized  $t_{2g}$  electrons of the manganite. These large magnetoresistance values are high enough for encoding and reading magnetic bits in future oxide spintronic sensors.

## 1. Introduction

$\text{R}_{1-x}\text{A}_x\text{MnO}_3$  perovskite manganites (R stands for a rare-earth ion and A for an alkaline earth ion), are known to exhibit a wealth of different responses due to the entanglement between spin, charge, and orbital degrees of freedom, which can be tuned to large extent by the band filling,  $x$ . The well-known colossal magnetoresistance (CMR) effect, describing dramatic changes of the electrical resistance ( $R$ ) upon application of magnetic field, is an example. It results from the competition between a metallic and a ferromagnetic state settled by the double exchange interaction and an antiferromagnetic insulating state driven by charge and orbital order.<sup>[1]</sup> In the conducting state, an external magnetic field aligns the nearly localized Mn 3d  $t_{2g}$ , and the nearly free  $e_g$  spins resulting in a half-metallic conduction band with nearly 100% spin polarization.<sup>[2]</sup> While colossal magnetoresistance requires large magnetic fields, thus hindering its implementation

G. Orfila, F. Cuellar, S. Rodriguez-Corvillo, S. López, A. Peralta, F. Gallego, J. Tornos, V. Rouco, Z. Sefrioui, L. Perez, A. Rivera-Calzada, C. Leon, J. Santamaria  
GFMC, Department Física de Materiales, Facultad de Física  
Universidad Complutense  
Madrid 28040, Spain

D. Sanchez-Manzano, S. J. Carreira, J. E. Villegas  
Unité Mixte de Physique  
CNRS  
Thales  
Palaiseau 91767, France

A. Arora, S. Valencia  
Department Spin and Topology in Quantum Materials  
Helmholtz-Zentrum Berlin für Materialien und Energie  
12489 Berlin, Germany  
E-mail: sergio.valencia@helmholtz-berlin.de  
S. Ruiz-Gómez  
Physics of Quantum Materials  
Max Planck Institute for Chemical Physics of Solids  
01187 Dresden, Germany

 The ORCID identification number(s) for the author(s) of this article can be found under <https://doi.org/10.1002/adma.202211176>

© 2023 The Authors. Advanced Materials published by Wiley-VCH GmbH. This is an open access article under the terms of the Creative Commons Attribution License, which permits use, distribution and reproduction in any medium, provided the original work is properly cited.

DOI: 10.1002/adma.202211176

in technological applications, disordered (misaligned) spin textures such as those appearing at grain boundaries, constrictions, or domain walls<sup>[3–5]</sup> (DW) can be the source of low field magnetoresistance (LFMR) of interest in spintronic applications. Indeed, a modern generation of magnetic memories, such as the acclaimed race-track memory,<sup>[6,7]</sup> exploit the controlled generation and manipulation of domain walls to encode and retrieve information.<sup>[8,9]</sup> Half-metals are amenable for LFMR applications as large magnetoresistance signals can be expected from spin accumulation at spin textures. In this respect,  $\text{La}_{1-x}\text{Sr}_x\text{MnO}_3$  (LSMO) manganites are specially promising. These compounds are easy to grow in thin film form, have a Curie temperature above room temperature ( $T_c = 360$  K, for  $x = 1/3$ ) and are chemically stable, as opposed to other (scarce) half-metal candidates, like  $\text{CrO}_2$  or Heusler alloys. Yet, domain wall magnetoresistance (DWMR) in LSMO manganites is poorly understood and it has remained an open longstanding problem with large discrepancies in the reported values of the domain wall resistance-area (DWRA) products, spanning between  $10^{-11}$  and  $10^{-15}$   $\Omega$  m<sup>2</sup>. Moreover, these values are much larger than the DWRA theoretically expected within double exchange models, which have been proposed to be in the range  $10^{-17}$  and  $10^{-18}$   $\Omega$  m<sup>2</sup> based on bandwidth reduction, that is, increased scattering rate, due to the misalignment between spins along the DW.<sup>[10,11]</sup>

Despite the DWMR problem being revisited recurrently in the last decade,<sup>[4,5,10–16]</sup> the controversy has remained due to conflicting interpretations of experimental results. Many of the early works in micro- or nanowires did not show domain wall imaging thus lacking evidence for the presence of domain walls at tracks or constrictions. Moreover, it has been recently pointed out<sup>[12]</sup> that the largest values of  $10^{-11}$   $\Omega$  m<sup>2</sup>,<sup>[4,5]</sup> obtained in such micro/nano devices at or close to room temperature, may result from a dominant contribution of the CMR rather than from DWMR. Works performed in continuous films have yield values of DWMR in the lower range,  $\approx 10^{-15}$   $\Omega$  m<sup>2</sup>. This is the case of experiments in LSMO samples with perpendicular anisotropy, in which the direction of an in-plane field leads to a configuration of maze domains with DWs either aligned parallel or perpendicular to the current direction.<sup>[16]</sup> In these experiments, in which many domains exist in the measured devices, the DWMR is estimated by normalizing the measured MR to an estimated number of domain walls across the current path. However, the interpretation of these results needs to be handled with care. An inherent problem associated to the use of macroscopic (millimeter size) samples is the tendency of LSMO manganites to nucleate small micron-size domains. The orientation of these domains with respect to the current cannot be assessed, nor their contribution to

the total magnetoresistance (MR) be evaluated. This encumbers data interpretation, as it prevents ascribing the electric transport results to particular domain wall configurations. Yet determining the actual strength of DWMR in LSMO is of major importance as high enough values could be of relevance for encoding and reading magnetic bits in future oxide spintronic sensors.

In this work we revisit the DWMR problem with a different strategy. By means of nanowire (NW) cross shaped samples, we tailor magnetic domain configurations with DWs precisely nucleated across the current path, as confirmed by space-resolved magnetic-sensitive microscopy techniques. Electric transport measurements, in conditions where CMR contribution can be ruled out, across individual DWs yield low field magnetoresistance values in excess of 10%. These values correspond to DWRA products in the range of  $10^{-11}$   $\Omega$  m<sup>2</sup>, which are three to four orders of magnitude larger than the values estimated in continuous films with multidomain states. This large magnetoresistance is analyzed in the light of non-equilibrium spin accumulation produced as spin-polarized charge carriers cross the DW separating non-colinear domains, and results of the difficulty of misoriented spins in half metals to adapt to the local magnetization orientation. These results will stimulate applications of domain wall engineering in spintronic devices.

## 2. Results and Discussion

20 nm epitaxial  $\text{La}_{0.7}\text{Sr}_{0.3}\text{MnO}_3$  thin films were epitaxially grown on (001)-oriented  $\text{SrTiO}_3$  (STO) by pure oxygen sputtering (see Experimental Section). Cross shape nanowire structures were defined by electron beam lithography and wet etching. The central (horizontal) nanowire, along which the electrical current is injected, had widths of 65, 180, and 500 nm for the three nanostructures analyzed. Two transverse electrical leads cross the NW. Those are used as voltage probes, and are 200 nm wide in all the studied devices. The temperature dependence of the longitudinal resistivity of the wires was similar to (unpatterned) LSMO films indicating that nanofabrication did not degrade the LSMO properties (see Figure S1, Supporting Information). LSMO has biaxial anisotropy with [110] easy axes. The central nanowire and the transverse leads are oriented along [100] and [010] LSMO magnetic hard axis directions. This device geometry allowed to measure the resistance of the nanowire region comprised between the 2 transverse leads (4-probe configuration), see **Figure 1a**. As it will be discussed below, the interplay between magnetocrystalline energy and magnetostatic interactions at the cross-shaped intersection (hereafter the cross) between the NW and the transverse leads triggers the nucleation of single domain walls at the intersections, allowing a neat measurement of its contribution to the magnetoresistance.

In the following we demonstrate by means of magnetic-sensitive space-resolved imaging, that is, magnetic force microscopy (MFM) and X-ray photoemission electron microscopy (XPEEM), that, upon cycling the magnetic field applied along the NW, the nucleation of single domain wall occurs via magnetization rotation at NW/traverse leads crossings.

Magnetic force microscopy has been taken at a temperature ( $T$ ) of 50 K for magnetic fields applied in the direction of the LSMO nanowire, see **Figure 1**. We note that MFM contrast is due to the strong stray fields generated by the local magnetization.

J. J. Riquelme, C. Munuera, F. J. Mompean, M. Garcia-Hernandez  
Departamento de Sistemas con baja dimensionalidad  
Instituto de Ciencia de Materiales de Madrid (ICMM), CSIC  
28049 Cantoblanco, Spain

J. J. Riquelme, C. Munuera, F. J. Mompean, M. Garcia-Hernandez,  
Z. Sefrioui, A. Rivera-Calzada, C. Leon, J. Santamaria  
Unidad Asociada UCM/CSIC  
Laboratorio de Heteroestructuras con aplicación en spintrónica  
28140 Madrid, Spain

L. Perez  
Instituto Madrileño de Estudios Avanzados – IMDEA Nanoscience  
28049 Madrid, Spain

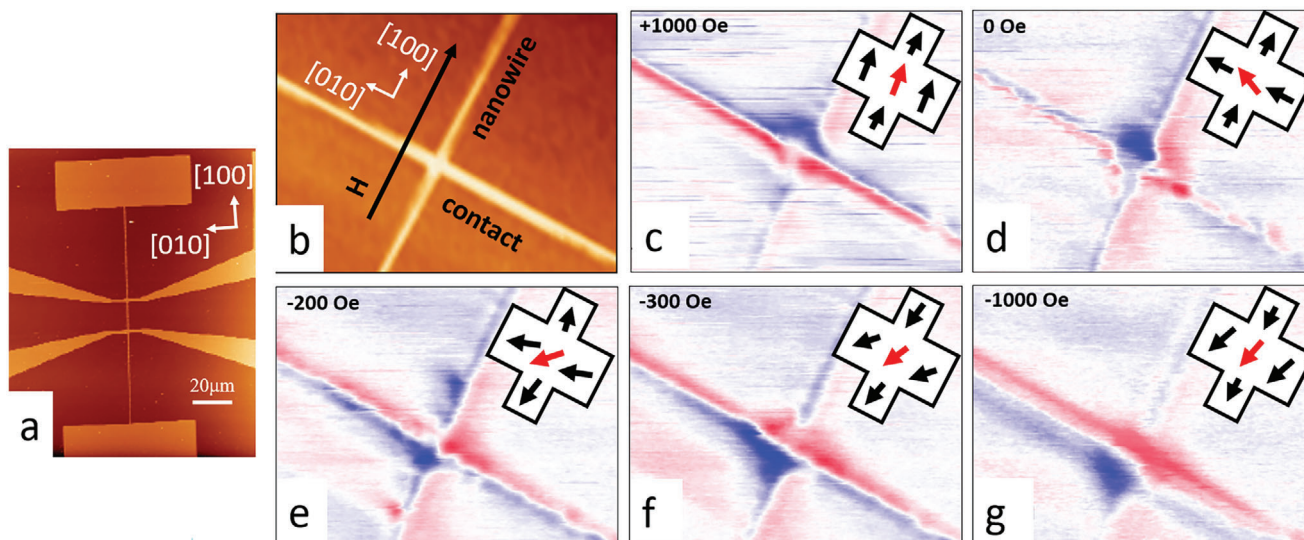


**Figure 1.** a) Atomic force microscopy (AFM) topographic image of a 180 nm nanowire with two additional 200 nm perpendicular leads acting as voltage contacts. b) AFM topographic image of the cross formed between the nanowire and the contact lead. c–g) MFM image of the stray field in the device for different in plane magnetic fields applied in the nanowire direction. The sketches at the upper right corner of the images show the magnetization direction in wire and contact lead.

Given the current experimental geometry, magnetization components parallel to the nanowire produce no magnetic poles and can thus, not be detected by MFM. Hence, MFM cannot resolve whether the magnetization of the wire is oriented along the  $[100]$  or  $[-100]$  direction. It can however be used to track the evolution of the orientation of the magnetization at the cross as function of an external magnetic field ( $H$ ). Starting at  $H = +1000$  Oe, LSMO nanowire and transverse leads are both uniformly magnetized in the direction of the field ( $[100]$  direction in coordinates depicted in Figure 1). This produces strong (weak) MFM contrast in the transverse leads (wire) since they are magnetized along their shortest (longest) dimension, see Figure 1c. Sweeping the magnetic field down toward zero leads to a rotation of the magnetization of the cross toward the  $[110]$  direction of the contact (Figure 1d). At  $H = -200$  Oe (Figure 1e) the magnetization at the cross is along the  $[-110]$  direction what stabilizes a domain wall at its intersection with the nanowire. Further increasing the negative magnetic field drags the magnetization at the cross (and at the wire) toward the  $[-100]$  direction (Figure 1f) and eventually saturates (Figure 1g). Notice the decrease of the MFM contrast in the nanowire reflecting the alignment of the magnetization with its direction. Magnetization switching in the nanowire shown in Figure 1f will be confirmed by XPEEM as discussed immediately below. These data offer clear evidence of a stepwise rotation of the magnetization at the cross as the magnetic field applied along  $[100]$  direction is swept between  $\pm 1000$  Oe.

To address the orientation of the magnetization direction at the wire during the magnetic field sweep and in order to evaluate the relative orientation of the magnetization at both sides of the domain walls at the cross we have performed XPEEM employing X-ray magnetic dichroism (XMCD) as magnetic contrast mechanism. As opposed to MFM, XMCD is proportional to the projection of the magnetization along the beam propagation direction. The experimental geometry has been set so to have maximum magnetic sensitivity along the direction set by the wire

(see Experimental Section). As in MFM, the in-plane magnetic field is applied along  $[100]$  (Figure 2a). Figure 2 depicts XMCD images obtained at  $T = 50$  K at the Mn  $L_3$  edge (641.8 eV). A blue–white–red color scale has been selected to depict the XMCD. Blue/red colored regions correspond to areas with an in-plane component of the magnetization oriented along the wire direction  $[\pm 100]$ . The direction and size of this component are encoded by the color and its intensity. White colored regions with XMCD  $\approx 0$  correspond to regions where magnetization points along the  $[0 \pm 10]$  direction. To confirm the sensitivity of XMCD along the wire direction measurements with the X-ray beam directed perpendicular to the NW were also taken (see Figure S2, Supporting Information).

After saturating the magnetization along the  $[-100]$  direction with  $H = +750$  Oe, the orientation of the magnetization at the wire remains oriented along  $[-100]$  after sweeping the field down to  $H = 0$  Oe. At the cross, as observed by means of MFM, we observed a steady rotation toward the direction of the transverse lead (Figure 2b,c) as the field is swept to zero. At  $-250$  Oe, we observe the nucleation of a DW at intersection of the cross with the NW (Figure 2e) which triggers the full reversal of the wire magnetization direction (Figure 2f). Figure 2g,h depicts line profiles of the XMCD across the cross for the XMCD image depicted in Figure 2e along the NW and along the contact directions, respectively. At the cross the profiles show a clear XMCD plateau at values differing from those of the transverse leads and the NW, indicating a rotation of the magnetization orientation toward  $[-110]$  in agreement with MFM. XMCD images obtained at absolute magnetic field values slightly below 250 Oe evidence that magnetization of the cross rotates first and this triggers the inversion of the magnetization of the wire. Figure S3, Supporting Information, displays XPEEM images acquired at a magnetic field of 237 Oe. It shows the rotation of the cross moment, while preserving the magnetization direction of the wire, nucleating a  $135^\circ$  domain wall.

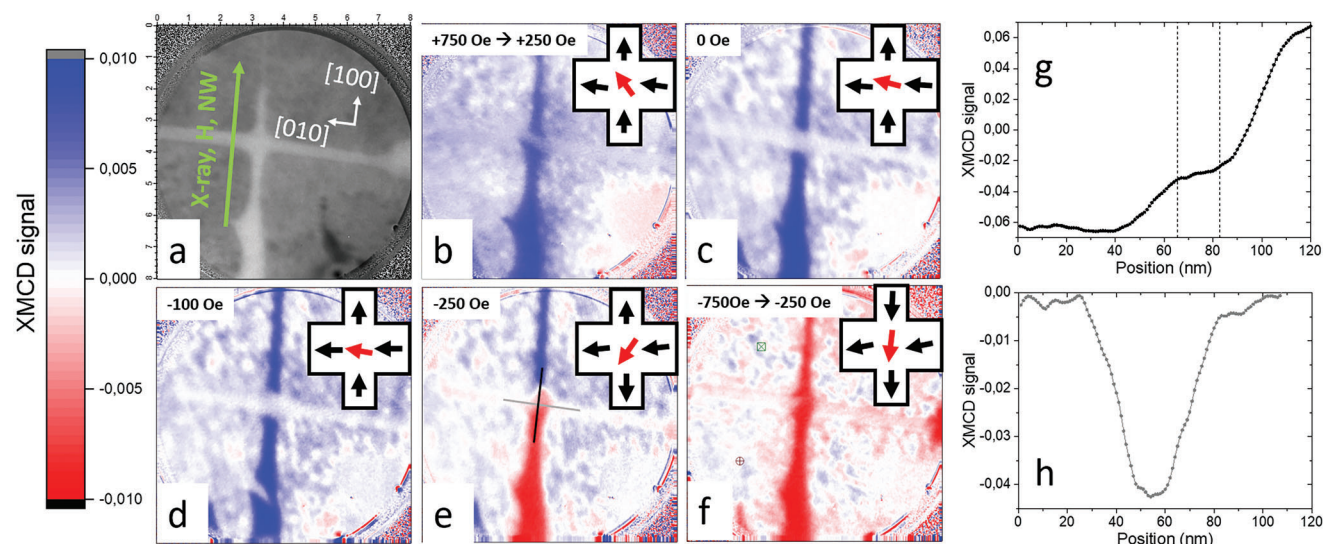


**Figure 2.** a) X-ray absorption image (XAS) image of the cross. X-ray beam and magnetic field are aligned along the nanowire (vertical) direction as indicated by the green arrow in (a). Field of view is  $8\ \mu\text{m}$ . b–f) XMCD images of the cross for different applied fields, blue (red) = magnetization (anti)parallel to the beam. g, h) Magnetization profile across the cross at  $H = -250\ \text{Oe}$  measured along the direction of the nanowire (g) and along the direction of the contact lead (h).

XMCD images obtained on a 105 nm wire show that, like the 180 nm wire, the reversal of magnetization at the cross after saturation triggers the nucleation of a pair of domain walls in the wire. This leads to the propagation of the walls at higher fields, as shown in Figure S4, Supporting Information. However, magnetization switching now occurs at higher field values (500 Oe) than in the 180 nm wire (150 Oe). Noteworthy, the maximum angle between magnetic moments on either side of the domain wall now reaches  $\approx 180^\circ$ .

This sequence of magnetic reversal, that is, rotation of the magnetization of the cross, nucleation of a domain wall, and its subsequent propagation triggering the reversal of the magnetiza-

tion at the wire is further confirmed by micromagnetic simulations (Figure 3).

The rotation of the magnetization at the cross can be explained by a competition between different anisotropies in the system. The biaxial magnetocrystalline anisotropy of LSMO tends to align the magnetic moment along the  $[\pm 1\pm 10]$  directions (see Figure S5, Supporting Information). Meanwhile the shape anisotropy of both, contact lead and nanowire, drags the magnetization along their respective  $[010]$  and  $[100]$  long directions. Compensation of the shape anisotropy at the cross favors the rotation of its magnetization, which switches between  $[\pm 1\pm 10]$  easy axes of LSMO and  $[\pm 100]$  and  $[0\pm 10]$  directions determined by the shape anisotropy

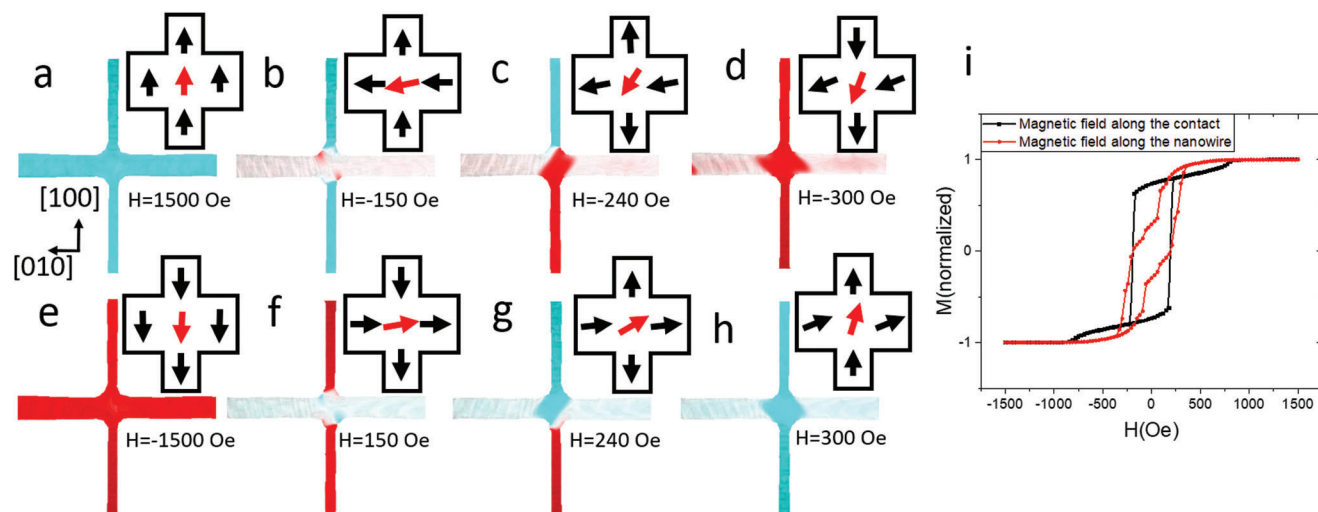


**Figure 3.** MuMax3 simulations of the magnetic state in function of applied magnetic field along the nanowire (vertical direction) from +1500 Oe to  $-1500\ \text{Oe}$ . a–h) Blue (red) colored areas denote magnetization (anti)parallel to the nanowire. i) Magnetic hysteresis loop along the nanowire and along the contact, showing the multiplicity of magnetic states.

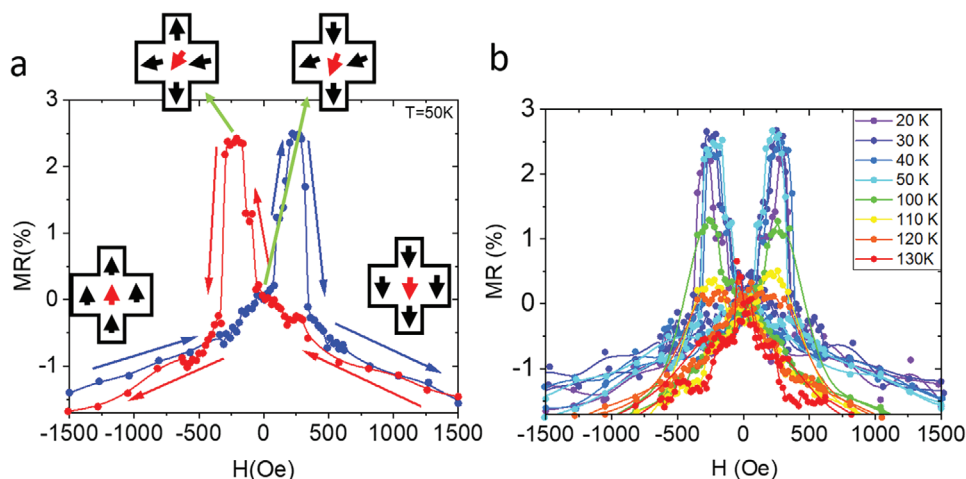


**Figure 4.** a) Magnetoresistance versus field  $MR(H)$  of a 180 nm-wide nanowire with magnetic field directed along the wire direction at  $T = 50$  K. Injected current was  $1 \mu\text{A}$ . Arrows in the sketches indicate the direction of the magnetization. b) Magnetoresistance at different temperatures between 20 and 130 K (see legend).

of NW and contact lead respectively (with some degree of rotation since the magnetic field is applied along the hard [100] magnetic axis of LSMO).

The independent rotation of the magnetization direction at the cross creates the opportunity to nucleate individual domain walls at its intersection with the nanowire. This allows to measure the DW contribution to the sample resistance and obtaining reliable values of the DWMR and of the DWRA product.

Magnetotransport measurements were performed for the 180 nm-wide nanowire studied by means of MFM and XPEEM (Figures 1 and 2). Four-points resistance versus field measurements were conducted at temperatures between 20 and 250 K injecting current along the nanowire and measuring voltage in the transverse leads with the in-plane magnetic field applied along the [100] wire long axis. In this configuration we probe the resistance of the wire segment between the transverse leads and the 2 DWs, one at each cross (see Figure S6, Supporting Information). Magnetoresistance is recorded while sweeping magnetic field after saturation. Upon crossing  $H = 0$  Oe, the wire resistance shows a sharp switching with high (magneto)resistance state plateaus between  $+150$  and  $+300$  Oe and between  $-150$  and  $-300$  Oe, see Figure 4a.

It should be noted that the high resistance plateaus occur at field values where both MFM and XPEEM have shown the nucleation and stabilization of a magnetic domain wall at the crosses due to the  $135^\circ$  misalignment between the magnetization at the cross and at the wire (Figure S3, Supporting Information). We can thus ascribe this high resistance state to the (see Figures 1f, 2c, and 3d) nucleation of a pair of high angle domain walls between the nanowire and the cross which appear as a result of the rotation of the magnetic moment of the cross. The domain wall magnetoresistance, defined as  $DWMR = (R(H) - R(0))/R(0)$  yields values close to 2.5% between 50 and 20 K, see Figure 4b. These MR values can be used to estimate the DWRA product. For a resistance increase ( $\Delta R$ ) of 3 k $\Omega$  (at 20 K in Figure 4b) and for a wire width of 180 nm and a sample thickness of 20 nm we obtain  $DWRA \approx 1.1 \times 10^{-11} \Omega \text{ m}^2$ , three to four orders of magnitude larger than the values reported for continuous LSMO films

with strain-induced perpendicular anisotropy. The DWRA value halves if each cross contributes with a DW (2 DWs in current path). The 2-step change in MR at the switching field is likely due to sequential nucleation of a DW at each cross.

Interestingly, DWMR values significantly increase when the width of the nanowire is reduced. Figure 5 shows a series of magnetoresistance curves obtained on a 65 nm-wide wire measured in the same conditions as the 180 nm wire. Note that the magnetic field range for which the high-resistance state can be observed is now much broader. The first switching field at  $T = 50$  K, leading to the high-resistance state, has significantly increased from  $\approx 150$  Oe (Figure 4) to  $\approx 500$  Oe. This increase is due to an enhanced contribution of the shape anisotropy of the wire. The second switching field, associated to the high- to low-resistance state switch, has also increased. In this case from  $\approx 300$  Oe to  $\approx 1600$  Oe. This is likely to be related to DW pinning by lateral inhomogeneities of the wire, which becomes dominant as the wire narrows. The strong pinning of the DW in the case of the 65 nm wire allows for observation of the DW magnetoresistance over a wide magnetic field range where the increase of (reverse) magnetic field compensates the shape-anisotropy field and favors magnetization rotation in the nanowire. The resulting reduction of the angle between spins at both sides of the DW explains the steady decrease of MR observed between the two switching fields. This effect is not observed in the 180 nm wire because the pinning effect of the domain wall is much weaker (notice the much narrower magnetoresistance plateau). For the 65 nm-wide NW we have measured DWMR at 20 K in excess of 10% which for a resistance increase  $\Delta R$  of 9 k $\Omega$  at low temperature, yields resistance area products of  $DWRA = 1.3 \times 10^{-11} \Omega \text{ m}^2$ , similar to those of the 180 nm wire.

The DWRA values obtained in our study are similar to those measured by Wolfman et al. and Arnal et al. (refs. [4] and [5], respectively) near room temperature. However, these previous measurements appear to be affected by contributions from colossal magnetoresistance (CMR) and anisotropic magnetoresistance (AMR).<sup>[12]</sup> In our case, contributions to the CMR or anisotropic

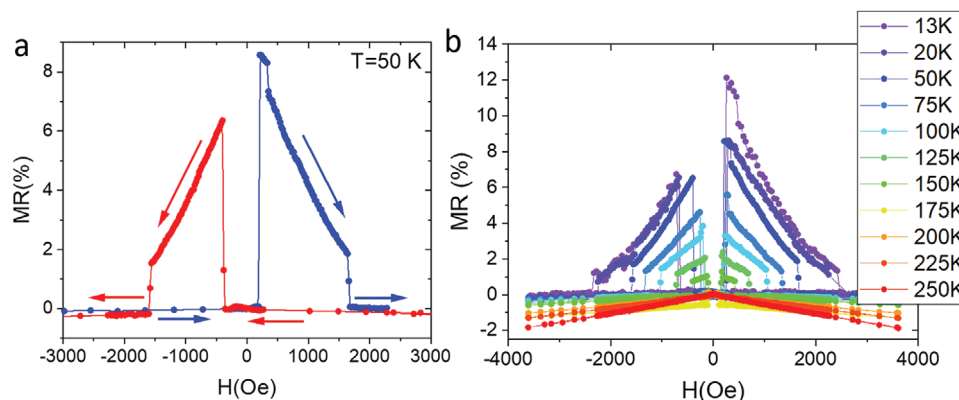


**Figure 5.** a) Magnetoresistance versus field  $MR(H)$  of a 65 nm-wide nanowire with magnetic field directed along the wire direction at  $T = 50$  K. Injected current was  $0.3 \mu\text{A}$ . Arrows in the sketches indicate the direction of the magnetic sweep. b) Magnetoresistance at different temperatures (see legend).

magnetoresistance to the large MR values observed can be discarded. Temperature dependent measurements show a steady decrease of the MR as  $T$  is increased, until it vanishes at 175 K. This is opposite to the behavior expected from CMR which would increase with temperature as the metal to insulator transition is approached. Concerning AMR, the size of the MR measured, in excess of 10%, is much larger than the values expected for AMR in manganites which are typically below 1%. In addition, the zero-field and the high-resistance state correspond to magnetization configurations for which the magnetic moment of the cross points (nearly) along  $[\pm 110]$  easy axis directions, so that AMR, depending on the cosine squared of the angle between current and magnetization, should not yield any resistance difference between both magnetic configurations.

Broader wires do show MR values well in the range of typical AMR values found in manganites. This is the case of 500 nm-wide wires with MR values of the order of 0.1% (see Figure S7, Supporting Information). This value is similar to the 0.16% magnetoresistance found in curved 2 micron wide LSMO wires, which was also ascribed to domain walls and discussed in terms of AMR.<sup>[17]</sup>

We next discuss the physical origin of the large magnetoresistance measured for 180 and 65 nm wide wires and ascribed to the presence of domain walls. Interesting insights can be obtained from the scaling of the magnetoresistance with the geometry of the domain wall. The width of the domain wall can be estimated in terms of the exchange interaction  $J$  and the anisotropy energy  $K$  as  $\delta_{\text{DW}} = \pi S \sqrt{\frac{J}{aK}}$ , where  $a$  is the lattice parameter and  $S$  the total spin of the Mn ion. Taking  $J = 2.3$  meV,<sup>[18,19]</sup>  $K = -(1.5-3.7) \times 10^4$  J m<sup>-3</sup>,<sup>[20,21]</sup>  $S = 3.7/2$ , and  $a = 0386$  nm we obtain  $\delta_{\text{DW}} \approx 30-50$  nm in good agreement with previous reports.<sup>[22]</sup> Estimates of the DW width from micromagnetic simulations yielded values of 60 nm for both 65 and 180 nm wires in reasonable agreement with the ones obtained from material's parameters. If the experimental magnetoresistance values (2.5% and  $\approx 10\%$  for 180 nm and 65 nm wires, respectively) are scaled to the relative size of the domain wall and wire length between contacts (15  $\mu\text{m}$ ), unexpectedly high values of 100% and 800% result for the relative change of the resistivity. This indicates that the relevant length scale in the problem is not the width of the domain wall and hints

that spin accumulation relaxing over a much larger length scale may be the relevant process. Moreover, the increase of MR as the NW width is reduced can also not be explained by confinement effects, proposed to be important in constrictions of dimensions smaller than the nominal width of the domain wall.<sup>[23]</sup> The width of the wires here investigated are larger or at least comparable to the estimated DW width.

We propose that the resistivity enhancement at domain walls can be discussed in terms of the mistracking effect,<sup>[24]</sup> where transport electron spins cannot follow the local magnetization texture in the domain wall. This non-adiabatic contribution is in fact responsible of so-called spin-torques leading to domain wall motion.<sup>[25]</sup> As a consequence of this mistracking,<sup>[26]</sup> spin channel mixing and spin accumulation occurs over the length scale of the domain wall width ( $\delta_{\text{DW}}$ ) and over the (longer scale) spin diffusion length ( $l_{\text{SF}}$ ), respectively. It is worth remarking that spin accumulation results from non-equilibrium spin populations, and it is typically achieved in spintronic devices by injecting current across ferromagnetic interfaces. Here, on the contrary, spin accumulation results from the mistracking of the spin texture at the domain wall by the electron spins of the current. An upper limit of the excess resistance of the domain wall due to spin accumulation can be estimated following the theoretical predictions discussed by Ieda et al.<sup>[27]</sup> The domain wall magnetoresistance can be expressed as<sup>[27]</sup>  $\frac{\Delta R}{R} = \frac{2P^2}{1-P^2} \frac{l_{\text{SF}}}{l_{\text{FM}}} F\left(\frac{\delta_{\text{DW}}}{l_{\text{SF}}}\right)$ , where  $P$  is the spin polarization,  $l_{\text{FM}}$  is the length of the ferromagnet (i.e., the distance between contacts in our case) and  $F\left(\frac{\delta_{\text{DW}}}{l_{\text{SF}}}\right)$  is a function describing the local modulation of the magnetization due to the accumulated spins which is 1, for an abrupt domain wall, and decays slowly when the width of the domain wall increases. In half metals the fast (hundreds of femtoseconds) spin flip route characteristic of metals, the Elliott-Yafet mechanism, caused by spin orbit driven spin mixing at high symmetry points, is blocked resulting of the vanishing minority spin density of states at the Fermi level. There is no spin channel for spin flip scattering and the energy has to be transferred through the less efficient spin lattice relaxation with a longer time scale ( $\tau_{\text{SF}} \approx 200-400$  ps).<sup>[28-30]</sup> This allows estimating the spin diffusion length for LSMO from the well-known expression  $l_{\text{SF}} = \sqrt{\frac{1}{3} v_{\text{F}} l \tau_{\text{SF}}}$ , assuming values for

the Fermi velocity  $v_F = 4 \times 10^5 \text{ m s}^{-1}$ <sup>[31]</sup> and mean free path  $l \approx 2\text{--}3 \text{ nm}$  and  $\tau_{SF} \approx 200\text{--}400 \text{ ps}$ . We obtain  $l_{SF} \approx 250\text{--}400 \text{ nm}$ , larger than the  $l_{SF} = 60 \text{ nm}$  reported for example for Co<sup>[32]</sup> where both spin channels mix due to spin orbit interaction. This value is larger than the estimated width of the domain wall (30–50 nm) what yields  $F(\frac{\delta_{DW}}{l_{SF}}) \approx 1$ .<sup>[27]</sup> Notice that in this limit the expression of the domain wall magnetoresistance approaches the one proposed by Valet and Fert for an abrupt domain wall.<sup>[33]</sup> For our experiment  $\frac{\Delta R}{R}$  varies between 6% and 12% for the 65 nm wire (Figure 5), and keeping in mind that the length of the ferromagnet between contacts is 15  $\mu\text{m}$ , a spin polarization  $P \approx 75\text{--}90\%$  is estimated, which is realistic for an LSMO nanowire at 20 K and in agreement with the values obtained previously in magnetic tunnel junctions.<sup>[34]</sup> The reasonable values of the spin polarization obtained in application of the model is reassuring that the mistracking scenario accounts for the observed magnetoresistance.

The decrease of magnetoresistance when temperature is increased obeys mainly to a loss of spin polarization which is known to scale with magnetization<sup>[35]</sup> when Curie temperature  $T_C$  is approached as  $M = M(0)[1 - (\frac{T}{T_C})^2]^{1/2}$ , where  $M(0)$  is the low temperature magnetization. Notice, however, that the domain wall magnetoresistance of the nanowires is suppressed before the Curie temperature, and it is overshadowed by the AMR for temperatures in excess of 200 K. Finally, the increase of the DW magnetoresistance values when the width of the wires is reduced can be understood in terms of the expected increase of the mistracking effect when the domain wall angle increases from 135° for the 180 nm wire to 180° for the 65 nm wire. Indeed, models of transport across domain walls predict MR scaling with domain wall angle squared<sup>[24]</sup> or with the cosine of the DW angle<sup>[36]</sup> yielding somewhat weaker (though not unrealistic) dependences of MR or DW angle than the ones experimentally observed.

### 3. Conclusions

The controlled inversion of the magnetization in a manganite nanowire observed by combined magnetic force microscopy and photoelectron microscopy imaging has enabled measuring transport across a single magnetic domain wall. We have found abrupt switching of the magnetoresistance which reaches values in excess of 10% corresponding to DWRA resistance area products  $DWRA = 1.3 \times 10^{-11} \Omega \text{ m}^2$ . This is three orders of magnitude larger than the values reported for continuous LSMO films hosting many domain walls resulting in ill-defined orientation of current to the wall. These DMRA products are also much larger than those expected from double exchange models where increased scattering rate is expected from the reduction of bandwidth (increased density of states) resulting from the (roughly 1°) misalignment between spins along the domain wall. We argue that these large MR values result from the strong spin accumulation at the wall due to the half-metallic state of the manganite, allowing long lived spins in the diffusive regime due to long spin lattice relaxation time. The large magnetoresistance values found are comparable to those of other practical spintronic magnetoresistance sensors, and indicate a new path to engineer spintronic sensors and injectors based on the controlled nucleation and manipulation of individual domain walls in half metallic manganites.

### 4. Experimental Section

La<sub>0.7</sub>Sr<sub>0.3</sub>MnO<sub>3</sub> 20 nm thin films were epitaxially grown on SrTiO<sub>3</sub> (001) substrates in a pure oxygen high-pressure RF sputtering from stoichiometric ceramic targets. LSMO was deposited at 3.2 mbar oxygen pressure at a temperature of 900 °C. After growth samples were annealed in 900 mbar of O<sub>2</sub> for one hour at 750 °C to ensure full oxidation and optimum doping.

LSMO cross-shape nanowires were defined by electron beam lithography in an RAITH 50 system with an LaB<sub>6</sub> cathode using the negative resist Ma-N2409. A wet etching process was used to minimize the damage of the transport properties of the LSMO wires (Figure 1a). Evaporated Ag spots were used to optimize contact to the wires.

Magnetoresistance measurements were performed in an He closed cycle cryostat equipped with a 4000 Oe electromagnet. Resistance was measured using 2 different instruments: a 2182 A nanovoltmeter with the 10 GΩ characteristic impedance at 1  $\mu\text{V}$  resolution (10 MΩ at 10  $\mu\text{V}$  resolution) and a 2400 source meter also with 10 GΩ input impedance. As the largest resistance values measured were in the range of 10<sup>5</sup> Ω for the 65 nm wire (see Figure S8, Supporting Information), voltmeter impedance was safely larger than sample resistance and did not require the use of electrometers to detect the voltage signals. Notice that for the sample used in this study, geometry current might leak to some degree into the contact leads at the cross, but since the DW nucleate in the nanowire at the cross this would equally affect  $R$  and  $\Delta R$ . Yet, the effect of uncontrolled current path was minimized in the thin nanowires used in this work as compared to other experimental measurements of domain wall magnetoresistance in the literature in either unpatterned samples or wider wires.

To avoid heating, current values were typically comprised between 0.1 and 1  $\mu\text{A}$  which yielded (for the 65 nm wire) current densities in the range 10<sup>3</sup> to 10<sup>4</sup> A cm<sup>-2</sup>. The effect of heating by the injected current was addressed exploiting the temperature dependence of the LSMO resistivity. Heating had been detected at current values in excess of 10  $\mu\text{A}$  though its effect was increasing the background resistance. See Figure S8, Supporting Information, showing measurements of the resistance of the 65 nm wire for different current levels comprised between 0.1 and 50  $\mu\text{A}$ . It was noticed that increasing current produced an increase of the resistance background level and decrease of the switching fields through the influence of heating effect. Also increased current yielded a reduction of the magnetoresistance effect more pronounced than the one expected from heating, indicating a current effect on the spin accumulation probably by spin torque.

The asymmetry between positive and negative branches of the magnetoresistance plots originated at some variability in the nucleation and depinning fields of the domain wall due to local (width) inhomogeneities of the 65 nm wire. Figure S8, Supporting Information, contains several successive magnetic field sweeps showing changes in switching fields and magnetoresistance plateaus. Asymmetries happened mostly at low temperature and disappear when temperature was increased as pinning effects of the domain wall became weaker.

Room temperature atomic force microscopy images were obtained in a commercial Bruker Nanoscope IIIA system. Simultaneous magnetic and topographic measurements were acquired with a low temperature magnetic force microscopy from Nanomagnetics Instruments Ltd. This system was compatible with a homemade cryostat, designed to fit in a commercial variable temperature insert (American Magnetics Inc.), equipped with a homemade 3-axis superconducting magnet which can apply up to 5 T out of plane fields and up to 1.2 T in plane magnetic fields in a temperature range comprised between 300 to 1.8 K.<sup>[37]</sup> MFM images were obtained in dynamic mode, with the tip scanning twice the sample surface at two different distances. A first scan was performed at distances of few nm to extract the topographic profile. Subsequently, the tip was retracted and the same profile was scanned at a tip-surface distance of 100 nm. The long-range magnetic interaction caused a phase shift of the cantilever oscillation. Images shown in this work were obtained at 50 K, using commercial tips from Nanosensors (PPP-MFMR). Prior to MFM measurements, the tips were magnetized with an external field (500 Oe) in their axial direction. Measurements were done with applied magnetic field after verifying that,

for the range of applied fields used (between  $\pm 1000$  Oe) the tip preserved the axial magnetization.

The magnetic state of the nanowires had been monitored by means of X-ray photoemission electron microscopy using X-ray magnetic circular dichroism as magnetic contrast mechanism in the XPEEM station at the UE49/PGMa beam line of the synchrotron radiation source BESSY II of the Helmholtz-Zentrum Berlin.<sup>[38]</sup> The sample was mounted on a sample holder capable of providing in plane magnetic field pulses of up to  $H = \pm 1000$  Oe. XMCD magnetic imaging was possible at lower magnetic fields in the interval  $H = \pm 350$  Oe. Images had been collected at the Mn  $L_3$ -edge (641.8 eV) for incoming circularly polarized radiation with right ( $\sigma^+$ ) and left ( $\sigma^-$ ) helicity, respectively. The beam impinged the sample at  $16^\circ$  grazing incidence angle from the wire direction. Under this condition, XMCD, which is proportional to the projection of the magnetization along the beam propagation direction, was mostly sensitive to in-plane magnetization. The data had been normalized to a background image and drift corrected before their averaging. The XMCD images were calculated as  $(\sigma^- - \sigma^+)/(\sigma^- + \sigma^+)$ . X-ray absorption spectroscopy ( $XAS = (\sigma^- + \sigma^+)/2$ ) and XMCD images were acquired at  $53 \pm 2$  K, the same temperature as the magnetoresistance switching. XMCD images depicted in Figure 2 and Figure S3, Supporting Information, were obtained during “multibunch” operation (ring current = 300 mA, 201 bunches). XMCD images depicted in Figure S4, Supporting Information, were obtained during “single bunch” operation. In this case, the photon beam was delivered by a single electron bunch with an intensity of 15 mA. Under these conditions charging effects, affecting imaging and focus, were severe. To minimize these effects, the device depicted in Figure S4, Supporting Information, was grown on top of an Nb-doped STO substrate. Front-end apertures were minimized reaching a compromise between focus conditions and enough signal.

The angular distribution of the magnetization depicted in Figure S3c, Supporting Information, had been computed from the XMCD images obtained at two orthogonal azimuth angles of the sample. For the sake of clarity panel (c) shows the device area only, after removing the noisy substrate region.

Micromagnetic simulations were performed with the software MuMax3<sup>[39]</sup> using a low-end graphic GPU (GeForce GTX1060). The nanowire and contact geometry were defined using the AFM images as a mask. The thickness of the simulated material was 20 nm. The simulations were performed in a slab with a voxel size of 4 nm in X, Y, and Z directions. The biaxial anisotropy of the system was introduced in the simulations as a cubic anisotropy along the (110) and ( $-110$ ) directions with a negative anisotropy constant of  $10^4$  J m $^{-3}$ .<sup>[40]</sup> The material constants employed for the saturation magnetization and the exchange stiffness were  $M_s = 400 \times 10^3$  A m $^{-1}$  and  $A_{ex} = 3 \times 10^{-12}$  J m $^{-1}$ . Hysteresis loops in the range  $\pm 1500$  Oe were simulated with the magnetic field in the direction of the nanowire, with a 5% offset to account for the experimental conditions.

## Supporting Information

Supporting Information is available from the Wiley Online Library or from the author.

## Acknowledgements

G.O. and D.S.-M. contributed equally to this work. The authors acknowledge received funding from the project To2Dox of FlagERA ERA-NET Cofund in Quantum Technologies implemented within the European Union's Horizon 2020 Program. This work was supported by Spanish AEI through grants, PID2020-118078RB-I00, PID2020-11556RB-I00 and PID2020-117024GB-C43 and by Regional Government of Madrid CAM through SINERGICO project Y2020/NMT-6661 CAIRO-CM. S.R.-G. also gratefully acknowledges the financial support of the Alexander von Humboldt foundation. Work at CNRS/Thales supported by French ANR-22CE30-0020 “SUPERFAST”. J.J.R was supported by the CSIC program for the Spanish Recovery, Transformation and Resilience Plan funded by the

Recovery and Resilience EU Facility EU regulation 2020/2094. The authors thank the Helmholtz-Zentrum Berlin für Materialien und Energie for the allocation of synchrotron radiation beamtime.

Open access funding enabled and organized by Projekt DEAL.

## Conflict of Interest

The authors declare no conflict of interest.

## Data Availability Statement

The data that support the findings of this study are available from the corresponding author upon reasonable request.

## Keywords

domain wall resistance, magnetoresistance, manganites, nanomagnetism, spintronics

Received: November 30, 2022

Revised: March 13, 2023

Published online: July 11, 2023

- [1] Y. Tokura, *Rep. Prog. Phys.* **2006**, *69*, 797.
- [2] J. H. Park, E. Vescovo, H. J. Kim, C. Kwon, R. Ramesh, T. Venkatesan, *Nature* **1998**, *392*, 794.
- [3] N. D. Mathur, G. Burnell, S. P. Isaac, T. J. Jackson, B. S. Teo, J. L. MacManus-Driscoll, L. F. Cohen, J. E. Evetts, M. G. Blamire, *Nature* **1997**, *387*, 266.
- [4] J. Wolfman, A. M. Haghiri-Gosnet, B. Raveau, C. Vieu, E. Cambril, A. Cornette, H. Launois, *J. Appl. Phys.* **2001**, *89*, 6955.
- [5] T. Arnal, A. V. Khvalkovskii, M. Bibes, B. Mercey, P. Lecoeur, A. M. Haghiri-Gosnet, *Phys. Rev. B: Condens. Matter Mater. Phys.* **2007**, *75*, 220409.
- [6] S. S. P. Parkin, M. Hayashi, L. Thomas, *Science (80-)*. **2008**, *320*, 190.
- [7] S. Parkin, S. H. Yang, *Nat. Nanotechnol.* **2015**, *10*, 195.
- [8] Z. Luo, A. Hrabec, T. P. Dao, G. Sala, S. Finizio, J. Feng, S. Mayr, J. Raabe, P. Gambardella, L. J. Heyderman, *Nature* **2020**, *579*, 214.
- [9] D. A. Allwood, G. Xiong, C. C. Faulkner, D. Atkinson, D. Petit, R. P. Cowburn, *Science (80-)*. **2005**, *309*, 1688.
- [10] N. D. Mathur, P. B. Littlewood, N. K. Todd, S. P. Isaac, B. S. Teo, D. J. Kang, E. J. Tarte, Z. H. Barber, J. E. Evetts, M. G. Blamire, *J. Appl. Phys.* **1999**, *86*, 6287.
- [11] L. Brey, arXiv: cond-mat/9905209, **1999**.
- [12] M. K. Wu, J. R. Ashburn, C. J. Torng, P. H. Hor, R. L. Meng, L. Gao, Z. J. Huang, Y. Q. Wang, C. W. Chu, *Phys. Rev. Lett.* **1987**, *58*, 908.
- [13] Y. Wu, Y. Suzuki, U. Rüdiger, J. Yu, A. D. Kent, T. K. Nath, C. B. Eom, *Appl. Phys. Lett.* **1999**, *75*, 2295.
- [14] Y. Suzuki, Y. Wu, J. Yu, U. Ruediger, A. D. Kent, T. K. Nath, C. B. Eom, *J. Appl. Phys.* **2000**, *87*, 6746.
- [15] I. Pallecchi, A. Gadaleta, L. Pellegrino, G. C. Gazzadi, E. Bellingeri, A. S. Siri, D. Marré, *Phys. Rev. B: Condens. Matter Mater. Phys.* **2007**, *76*, 174401.
- [16] S. R. Bakaul, W. Hu, T. Wu, T. Kimura, *Phys. Rev. B: Condens. Matter Mater. Phys.* **2012**, *86*, 184404.
- [17] M. Foerster, L. Peña, C. A. F. Vaz, J. Heinen, S. Finizio, T. Schulz, A. Bisig, F. Büttner, S. Eisebitt, L. Méchin, S. Hühn, V. Moshnyaga, M. Kläui, *Appl. Phys. Lett.* **2014**, *104*, 072410.
- [18] R. Akiyama, H. Tanaka, T. Matsumoto, T. Kawai, *Appl. Phys. Lett.* **2001**, *79*, 4378.

- [19] T. Nagai, H. Yamada, M. Konoto, T. Arima, M. Kawasaki, K. Kimoto, Y. Matsui, Y. Tokura, *Phys. Rev. B: Condens. Matter Mater. Phys.* **2008**, *78*, 180414.
- [20] Y. Suzuki, H. Y. Hwang, S. W. Cheong, T. Siegrist, R. B. Van Dover, A. Asamitsu, Y. Tokura, *J. Appl. Phys.* **1998**, *83*, 7064.
- [21] G. Shibata, M. Kitamura, M. Minohara, K. Yoshimatsu, T. Kadono, K. Ishigami, T. Harano, Y. Takahashi, S. Sakamoto, Y. Nonaka, K. Ikeda, Z. Chi, M. Furuse, S. Fuchino, M. Okano, J. I. Fujihira, A. Uchida, K. Watanabe, H. Fujihira, S. Fujihira, A. Tanaka, H. Kumigashira, T. Koide, A. Fujimori, *npj Quantum Mater.* **2018**, *3*, 3.
- [22] K. J. OShea, D. A. MacLaren, D. McGrouther, D. Schwarzbach, M. Jungbauer, S. Hühn, V. Moshnyaga, R. L. Stamps, *Nano Lett.* **2015**, *15*, 5868.
- [23] P. Bruno, *Phys. Rev. Lett.* **1999**, *83*, 2425.
- [24] P. M. Levy, S. Zhang, *Phys. Rev. Lett.* **1997**, *79*, 5110.
- [25] C. Burrowes, A. P. Mihai, D. Ravelosona, J. V. Kim, C. Chappert, L. Vila, A. Marty, Y. Samson, F. Garcia-Sanchez, L. D. Buda-Prejbeanu, I. Tudosa, E. E. Fullerton, J. P. Attané, *Nat. Phys.* **2009**, *6*, 17.
- [26] U. Ebels, A. Radulescu, Y. Henry, L. Piraux, K. Ounadjela, *Phys. Rev. Lett.* **2000**, *84*, 983.
- [27] J. Ieda, S. Takahashi, M. Ichimura, H. Imamura, S. Maekawa, *J. Magn. Magn. Mater.* **2007**, *310*, 2058.
- [28] A. I. Lobad, R. D. Averitt, C. Kwon, A. J. Taylor, *Appl. Phys. Lett.* **2000**, *77*, 4025.
- [29] G. M. Müller, J. Walowski, M. Djordjevic, G. X. Miao, A. Gupta, A. V. Ramos, K. Gehrke, V. Moshnyaga, K. Samwer, J. Schmalhorst, A. Thomas, A. Hütten, G. Reiss, J. S. Moodera, M. Münzenberg, *Nat. Mater.* **2008**, *8*, 56.
- [30] Q. Zhang, A. V. Nurmikko, G. X. Miao, G. Xiao, A. Gupta, *Phys. Rev. B: Condens. Matter Mater. Phys.* **2006**, *74*, 064414.
- [31] N. Mannella, W. L. Yang, X. J. Zhou, H. Zheng, J. F. Mitchell, J. Zaanen, T. P. Devereaux, N. Nagaosa, Z. Hussain, Z. X. Shen, *Nature* **2005**, *438*, 474.
- [32] L. Piraux, S. Dubois, A. Fert, *J. Magn. Magn. Mater.* **1996**, *159*, L287.
- [33] T. Valet, A. Fert, *Phys. Rev. B* **1993**, *48*, 7099.
- [34] J. Tornos, F. Gallego, S. Valencia, Y. H. Liu, V. Rouco, V. Lauter, R. Abrudan, C. Luo, H. Ryll, Q. Wang, D. Hernandez-Martin, G. Orfila, M. Cabero, F. Cuellar, D. Arias, F. J. Mompean, M. Garcia-Hernandez, F. Radu, T. R. Charlton, A. Rivera-Calzada, Z. Sefrioui, S. G. E. Te Velthuis, C. Leon, J. Santamaria, *Phys. Rev. Lett.* **2019**, *122*, 037601.
- [35] Y. Liu, F. A. Cuellar, Z. Sefrioui, J. W. Freeland, M. R. Fitzsimmons, C. Leon, J. Santamaria, S. G. E. Te Velthuis, *Phys. Rev. Lett.* **2013**, *111*, 247203.
- [36] T. Taniguchi, H. Imamura, *J. Phys. Conf. Ser.* **2011**, *266*, 012108.
- [37] J. A. Galvis, E. Herrera, I. Guillamón, J. Azpeitia, R. F. Luccas, C. Munuera, M. Cuenca, J. A. Higuera, N. Díaz, M. Pazos, M. García-Hernandez, A. Buendía, S. Vieira, H. Suderow, *Rev. Sci. Instrum.* **2015**, *86*, 013706.
- [38] F. Kronast, S. Valencia, *J. Large-Scale Res. Facil.* **2016**, *2*, A90.
- [39] A. Vansteenkiste, J. Leliaert, M. Dvornik, M. Helsen, F. Garcia-Sanchez, B. van Waeyenberge, *AIP Adv.* **2014**, *4*, 107133.
- [40] K. Steenbeck, R. Hiergeist, *Appl. Phys. Lett.* **1999**, *75*, 1778.